

Electrical activity of Mg clustering at nanoscale defects induced by N ion implantation in GaN

Kosuke Ishikawa,¹ Emi Kano,² Jun Uzuhashi,³ Kensuke Sumida,¹ Tetsuo Narita,⁴ Masahiro Horita,¹ Junya Sahashi,¹ Shun Lu,² Jun Suda,¹ Tadakatsu Ohkubo,³ Tetsu Kachi,² Nobuyuki Ikarashi²

¹ Graduate School of Engineering, Nagoya University, Nagoya, Aichi 464-8603, Japan

² Institute of Materials and Systems for Sustainability, Nagoya University, Nagoya, Aichi 464-8601, Japan

³ National Institute for Materials Science, Tsukuba, Ibaraki 305-0047, Japan

⁴ Toyota Central R&D Labs., Inc., Nagakute, Aichi 480-1192, Japan

Corresponding author: Emi Kano

Email: kano@imass.nagoya-u.ac.jp

Abstract

The p-type doping of GaN using Mg ion implantation remains a critical challenge in the development of GaN power devices. Herein, we demonstrate that Mg clustering, induced by sequential N ion implantation, impacts acceptor concentration (N_a), compensating donor concentration (N_d), and acceptor activation energy (ΔE_a). N was implanted at the same concentration as Mg to suppress Mg diffusion. Hall-effect measurements indicated that, for Mg doses above $1 \times 10^{19} \text{ cm}^{-3}$, N_a reached a plateau whereas N_d continued to increase. Consequently, the net acceptor concentration ($N_a - N_d$) reached a maximum of $4 \times 10^{18} \text{ cm}^{-3}$ at a Mg dose of $1 \times 10^{19} \text{ cm}^{-3}$. ΔE_a decreased with increasing Mg dose. Atomic-resolution structural analyses revealed that nanoscale defects generated by N implantation induced Mg clustering around these defects, with the cluster density increasing with Mg dose. Notably, peak Mg concentrations within these clusters exceeded $1 \times 10^{21} \text{ cm}^{-3}$ and increased with Mg dose, whereas Mg atoms outside these clusters remained uniformly dispersed in the range $1.3\text{--}1.5 \times 10^{18} \text{ cm}^{-3}$ regardless of Mg dose. These findings suggest that the increase in N_a up to a Mg dose of $1 \times 10^{19} \text{ cm}^{-3}$ can be attributed to the Mg atoms within these Mg-rich clusters acting as acceptors, which also lowered ΔE_a . Conversely, Mg atoms at or near the peak Mg-concentration sites likely acted as compensating donors, contributing to the increase in N_d with increasing Mg dose. These findings elucidate the impact of Mg clustering induced by nanoscale implantation defects on the p-type conductivity of GaN, providing insight for improving ion-implantation doping strategies in GaN.

Ion implantation technology for the conductivity control of GaN-based devices has been extensively developed,¹⁻¹¹ with n-type doping being well-established and widely used in electronic device fabrications¹⁻³. In contrast, p-type doping is only now approaching practical implementation owing to recent advances in post-implantation activation annealing techniques.^{12,13} However, the fundamental mechanisms underlying acceptor activation in ion-implanted GaN remain unclear.

Annealing in a high-pressure N₂ atmosphere (500 MPa or higher) prevents the surface decomposition of the GaN substrate, even at temperatures exceeding 1300 °C,^{12,13} thereby enabling the electrical activation of ion-implanted Mg.^{12,14,15} However, this process induces the out-diffusion of Mg from the ion-implanted region, thereby reducing the Mg concentration within the implanted area.^{16,17} This concentration reduction remains a significant challenge for practical implementation. Recent studies have reported that sequential N implantation at a concentration comparable to that of Mg can help suppress this concentration reduction.¹⁸⁻²⁰

The crystal defects generated by sequential N implantation play a crucial role in maintaining the Mg concentration.²¹⁻²⁴ Specifically, the implantation process increases the density of point defects, which promotes a higher Mg_{Ga} concentration and thereby mitigates Mg concentration reduction in the ion-implanted region.²⁴ Furthermore, nanoscale defects generated by N implantation induce Mg clusters, preventing the reduction in Mg concentration observed in samples without N implantation.^{24,25} However, some of the Mg atom clusters at these nanoscale defects likely do not act as acceptors.²⁴ Therefore, defect-mediated Mg clustering significantly impacts the p-type electrical characteristics of ion-implanted GaN. The underlying mechanisms whereby these defects affect the electrical properties remain poorly understood, as systematic analyses are still lacking.

In this study, we demonstrate that crystal defect-induced Mg-rich clusters formed during ion implantation and activation annealing influence the acceptor concentration (N_a), compensating donor concentration (N_d), and acceptor ionization energy (ΔE_a) in GaN sequentially implanted with Mg and N ions. Mg and N were implanted at equal concentrations, with the Mg dose ranging from 3×10^{18} to $1 \times 10^{20} \text{ cm}^{-3}$. Temperature-dependent Hall-effect measurements revealed the implantation dose dependence of N_a , N_d , and ΔE_a . Transmission electron microscopy (TEM) and atom probe tomography (APT) analyses revealed the defect structures and Mg atom distribution with atomic-scale resolution. These analyses elucidate the impact of crystal defect formation and the resulting Mg clustering on N_a , N_d , and ΔE_a in the samples.

Mg and N ions were sequentially implanted into a 3- μm -thick n-type GaN epitaxial layer ($[\text{Si}] = 2 \times 10^{16} \text{ cm}^{-3}$) grown on freestanding GaN (0001) substrates to form 400-nm-depth box-shaped profiles. Four samples, hereinafter referred to as Samples A–D, were prepared with Mg implantation doses of 3×10^{18} , 1×10^{19} , 3×10^{19} , and $1 \times 10^{20} \text{ cm}^{-3}$, respectively. N ions were implanted to match the Mg concentration and profile of each sample. Post-implantation annealing was performed at 1300 °C

for 60 min in an N₂ atmosphere at 0.5 GPa.^{12,15} Ion implantation profiles were simulated using the scatGUI software.²⁶

Crystal defects were examined using annular dark-field (ADF) scanning TEM (STEM). The acceleration voltage was 200 kV, and the inner and outer angles of the ADF detector were 20 and 60 mrad, respectively. TEM specimens were prepared by mechanical thinning followed by Ar-ion milling. The TEM specimen thicknesses were determined by convergent beam electron diffraction analysis using the mbfit program.^{27,28}

APT measurements were performed using *CAMECA* Invizo6000 in the 257.5 nm DUV laser pulsing mode at a frequency of 440 kHz and a specimen temperature of 30 K. Using a focused ion beam system, we fabricated APT specimens to have a radius of curvature of 50 nm and a shank angle of 10°. ²⁹ All the specimens were then cleaned at 2 kV.³⁰

For the Hall-effect measurements, Ni (20 nm)/Au (100 nm) electrodes with a diameter of 600 µm were formed at the four corners of the square samples. Before electrode formation, a 50-nm-thick Mg layer was deposited at the electrode areas and annealed,³¹ reducing the resistance of the ohmic contact regardless of the doping concentrations of p-type GaN. Hall-effect measurements were conducted in the temperature range of 160–500 K. Details of the sample preparation for the Hall-effect measurements have been described in our previous report.³²

Figures 1(a)–(d) show the ADF-STEM images, indicating that the density of nanoscale crystal defects increases with the Mg implantation dose. The small bright dots in the images are defects generated during ion implantation and subsequent annealing.^{20,24} Two distinct types of defects can be observed regardless of the Mg implantation dose, as exemplified in Fig. 1(e) for Sample D. The first, denoted as Type 1, appears as a bright area with a central neck (indicated by the dashed line). This defect has been identified as an extrinsic dislocation loop with an additional GaN c-plane. Namely, an extra nano-scale disk of one GaN c-plane is inserted between the c-planes of GaN.²⁴ The second, denoted as Type 2, appears as a bright region divided into two sides by the dark area (dashed line) and is an extrinsic dislocation loop with an additional GaN a-plane.²⁴ The dashed lines in Fig. 1(e) indicate the approximate positions of the additional GaN planes.

Figures 1(f)–(j) show the 3D APT atom maps of Mg in the ion-implanted regions, where green dots represent individual Mg atoms. The top of each map is positioned several tens of nanometers below the GaN surface. These maps reveal the formation of nanometer-scale Mg-rich clusters, with a number density that increases with the Mg implantation dose. A previous study attributed such clustering to the strain fields associated with the defects shown in Figs. 1(a)–(d).²⁴ As an example, the Mg distribution around a cluster in Sample D is shown in the inset of Fig. 1(j). The doughnut-shaped morphology on the (0001) plane of GaN indicates that Mg clustering was induced by a Type 1 defect.²⁴ Furthermore, the APT analysis revealed that the peak Mg concentration within these

clusters was over $1 \times 10^{21} \text{ cm}^{-3}$. Figure 1(j) shows the Mg concentration depth profile extracted from the cylindrical volume indicated in the inset. The Mg concentration depth profile in Sample A is also indicated in the diagram. The peak concentrations for Samples A–D were typically 1.8×10^{21} , 1.6×10^{21} , 2.4×10^{21} , and $7.3 \times 10^{21} \text{ cm}^{-3}$, respectively. From Samples B to D, the peak concentration increased with increasing Mg implantation dose. Mg atom maps and corresponding concentration profiles of the Mg-rich clusters for Samples A–C are provided in Supplementary Material.

The APT analysis further showed that Mg atoms were uniformly or randomly dispersed outside the Mg-rich clusters, with a concentration range of $1.3\text{--}1.5 \times 10^{18} \text{ cm}^{-3}$ regardless of the Mg implantation dose (Fig. 2). This concentration was estimated using a binomial analysis of the APT data. In contrast, the density of the clustered Mg atoms, which is defined as the difference between the total and uniformly dispersed Mg concentrations, increased proportionally with the Mg implantation dose.

Figure 3 presents the Mg concentration depth profiles obtained using secondary ion mass spectrometry. The profiles show that Mg atoms diffused from the implanted region toward the substrate side, forming a layer with an Mg concentration range of $1\text{--}2 \times 10^{18} \text{ cm}^{-3}$. This concentration is nearly identical to that of the uniformly dispersed Mg atoms within the implanted region. For carrier concentration calculations, the effective film thickness was defined as the depth where the Mg concentration reduced to $1 \times 10^{17} \text{ cm}^{-3}$.

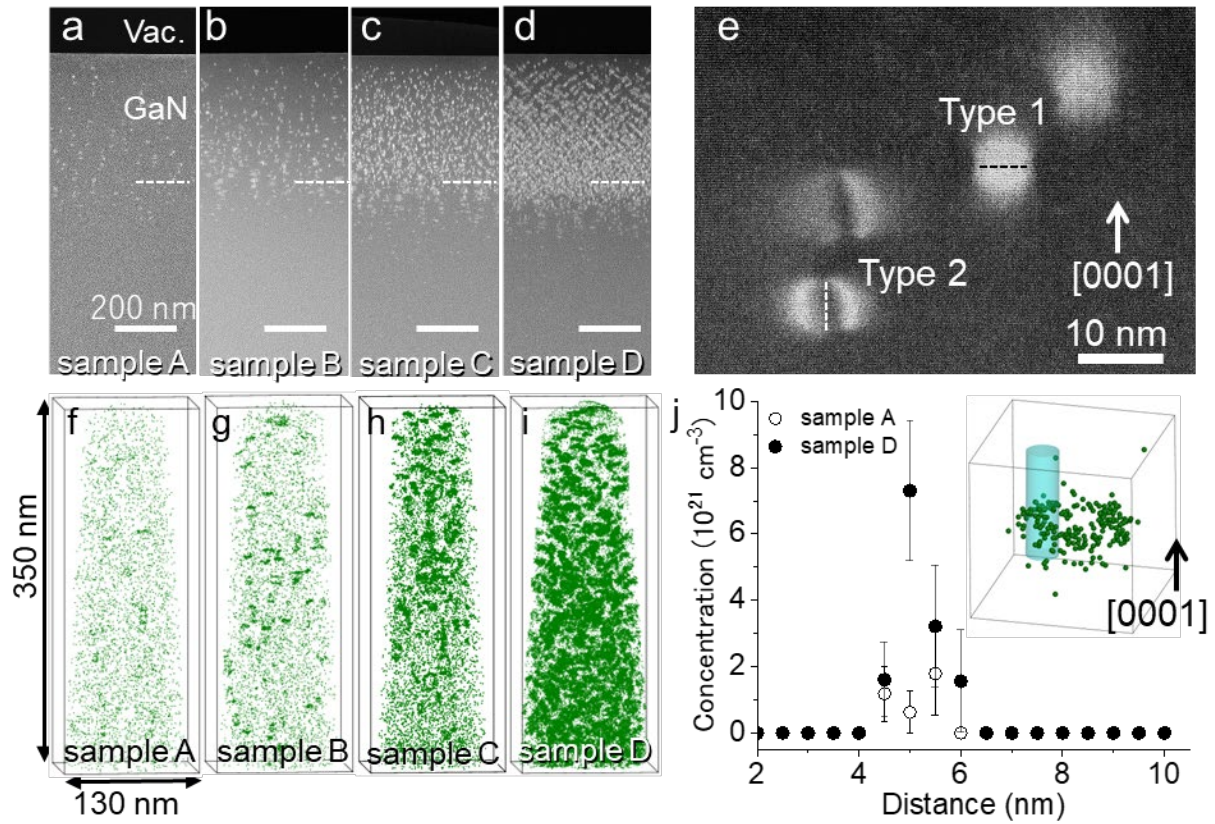


Fig. 1. (a)–(d) Cross-sectional annular dark-field scanning transmission electron microscopy (ADF-STEM) images of the ion-implanted regions in Samples A–D. The dashed lines indicate a depth of 400 nm from the GaN surface. The incident beam direction is $\langle 1-100 \rangle$, and the specimen thickness is approximately 100 nm. Crystal defects are observed as small bright dots; their number density increases with the Mg implantation dose. (e) Close-up of defects in Sample D. Two types of defects can be observed in all samples. Type 1: a bright area with a central neck (dashed line). Type 2: a bright area bisected by a dark region (dashed line). (f)–(i) Atom probe tomography (APT) 3D maps of Mg in the ion-implanted regions of Samples A–D. Green dots indicate individual Mg atoms. The density of Mg-rich clusters increases with the Mg implantation dose. (j) Representative Mg concentration profile around a Mg-rich cluster in Sample D. The inset shows the analyzed region (a 15 nm cube), where the concentration is measured within a cylindrical volume with a 3 nm diameter. Concentration is plotted as a function of the distance from the cylinder top (solid circles). The concentration profile across a Mg-rich cluster in Sample A is indicated by open circles. Both profiles exhibit peak concentrations exceeding $1 \times 10^{21} \text{ cm}^{-3}$.

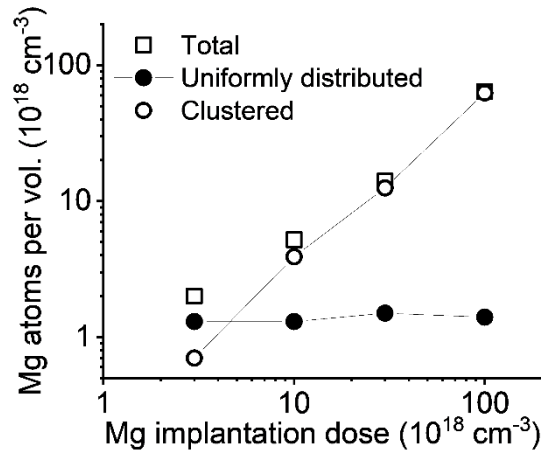


Fig. 2 Uniformly distributed and clustered Mg atoms in Samples A–D obtained through a binomial analysis of atom probe tomography (APT) data. The vertical axis indicates the number of Mg atoms per unit volume. The amount of uniformly dispersed Mg atoms is in the range $1.3\text{--}1.5 \times 10^{18} \text{ cm}^{-3}$ regardless of the Mg implantation dose, while that of the clustered Mg atoms increases monotonically. The numerical values for these Mg densities are provided in the Supplementary Material.

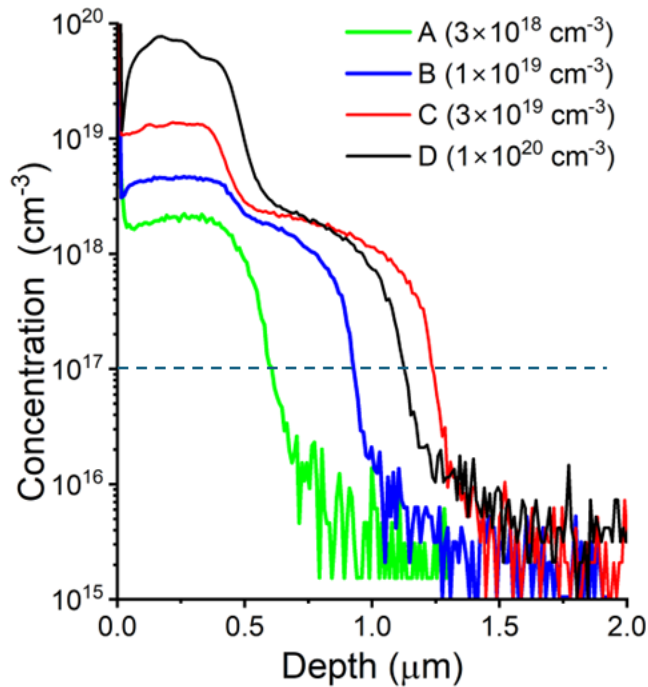


Fig. 3 Mg concentration depth profiles. Mg atoms diffuse from the 400-nm-thick implanted region, forming a layer with a concentration range of $1\text{--}2 \times 10^{18} \text{ cm}^{-3}$ on the substrate side. The letters A–D indicate different samples.

Room-temperature two-terminal current–voltage (I–V) characteristics were measured using the same structures as those employed for the Hall-effect measurement (Fig. 4a). The linear I–V curves for Samples A, B, and C demonstrate the formation of ohmic contacts via our contact fabrication process involving Mg deposition. In contrast, almost no current was detected for Sample D within the measured voltage range.

Hall-effect measurements were performed to investigate the dependence of N_a , N_d , and ΔE_a on the Mg implantation dose. Figure 4(b) shows the temperature-dependent carrier concentrations for Samples A to C (circles). While Samples A, B, and C exhibited p-type conductivity, Sample D did not. The solid lines represent theoretical fits based on the charge neutrality condition and semiconductor statistics, using N_a , N_d , and ΔE_a as fitting parameters. For these fits, an effective density of states at 300 K of $7.3 \times 10^{19} \text{ cm}^{-3}$ and a Hall scattering factor of $\gamma_H = 1$ were adopted.³³ The details of the analysis procedure, including fitting equations and parameters, are provided in the Experimental Methods section of Ref. 33. The resulting parameters are plotted in Fig. 4(c) and listed in Table S1 of the Supplementary Material. Figure 4(c) shows that N_a increases as the Mg dose rises from Samples A to B (3×10^{18} to $1 \times 10^{19} \text{ cm}^{-3}$) but levels off at $5.2 \times 10^{18} \text{ cm}^{-3}$ between Samples B and C (dose exceeding $1 \times 10^{19} \text{ cm}^{-3}$). In contrast, N_d increases monotonically with the Mg dose across Samples A to C. This leads to a maximum net acceptor concentration ($N_a - N_d$) of $4 \times 10^{18} \text{ cm}^{-3}$ at an Mg dose of $1 \times 10^{19} \text{ cm}^{-3}$ (Sample B), after which the concentration decreases due to the continuous rise in N_d . In addition, ΔE_a decreases with increasing Mg dose from Samples A to C.

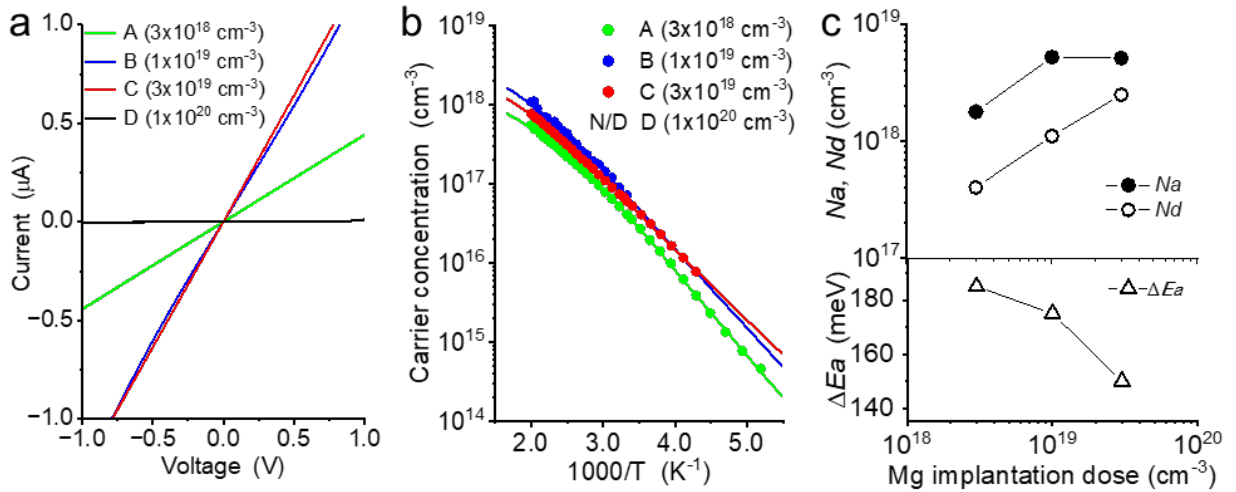


Fig. 4 (a) Two-terminal I–V characteristics. The current increases from Samples A to C with increasing Mg implantation doses, whereas Sample D exhibits a significantly lower current. (b) Temperature dependence of hole concentration. Solid circles and lines represent experimental data and fitting curves, respectively. The measurable temperature ranges vary depending on the experimental setup. (c) N_a , N_d , and ΔE_a as a function of the Mg implantation dose. N_a , N_d , and ΔE_a values are provided in the Supplementary Material.

Our analyses showed that, among Samples A and B, N_a was higher in Sample B (Fig. 4(c)). Concurrently, Mg concentrations in Samples A and B differed within the ion-implanted region (Fig. 3), attributed to the higher number density of the clustered Mg atoms in the implanted region of Sample B (Fig. 2). These findings indicate that a portion of the Mg atoms in the Mg-rich clusters acted as acceptors, increasing N_a in Sample B. This is further supported by the fact that N_a in Sample B ($5.2 \times 10^{18} \text{ cm}^{-3}$) significantly exceeded the Mg concentration both outside the Mg-rich clusters ($1.3 \times 10^{18} \text{ cm}^{-3}$) and within the underlying Mg-diffused layer ($1-2 \times 10^{18} \text{ cm}^{-3}$). In contrast, between Samples B and C, N_a remained identical (Fig. 4(c)), despite the higher number density of clustered Mg atoms in Sample C (Fig. 2). This implies that not all Mg atoms within these clusters acted as acceptors, which is consistent with our previous analyses of Mg and N ion implanted samples.²⁴

The Mg acceptors within Mg-rich clusters likely reduced the apparent ΔE_a of the samples. This is because the Mg concentration inside these clusters in Samples A–C was higher than that outside the clusters ($1.3-1.5 \times 10^{18} \text{ cm}^{-3}$) or in the Mg-diffused layer ($1-2 \times 10^{18} \text{ cm}^{-3}$) (Figs. 2 and 3) and because ΔE_a reportedly decreased with increasing N_a for N_a below $2 \times 10^{20} \text{ cm}^{-3}$.^{34,35} As we assumed a single ΔE_a value in our carrier concentration analysis, the presence of these low- ΔE_a acceptors lowered the apparent ΔE_a of the samples. Additionally, the peak Mg concentration in a Mg-rich cluster increased with increasing Mg dose (Fig. 1(j) and Fig. S2 in the Supplementary Material). This strongly suggests that the average Mg concentration in the clusters also increased, implying that ΔE_a of the Mg acceptors in the clusters decreased with increasing Mg dose. These results explain the observed dependency of the apparent ΔE_a on the Mg implantation dose.

The extremely high Mg concentration peaks (exceeding $1 \times 10^{21} \text{ cm}^{-3}$) observed within the Mg-rich cluster (Fig. 1(j)) strongly suggest that the Mg atoms distributed around these peaks acted as compensating donors. This is because a previous theoretical study showed that the formation energy of interstitial Mg (Mg_i) sharply decreased when the Mg concentration exceeded 10^{20} cm^{-3} , and such Mg_i s act as double donors that compensate for Mg acceptors.³⁶ Furthermore, the number density of these high-Mg concentration sites increased with the Mg implantation dose (Figs. 1(a)–(d) and (f)–(i)), implying a corresponding increase in the number density of Mg_i atoms. This suggests that the rise in N_d from Samples A to C can be partially attributed to the presence of Mg_i s within the Mg-rich clusters. Consequently, these findings reveal the amphoteric nature of Mg clustering: it contributes to increasing N_a and decreasing ΔE_a , while simultaneously promoting the formation of compensating donors. Furthermore, these results clarify that Mg clustering plays a crucial role in determining the net acceptor concentration, providing a fundamental basis for advancing ion-implantation doping technologies for GaN.

For Mg implantation doses exceeding $1 \times 10^{19} \text{ cm}^{-3}$, we found that the net acceptor concentration decreased while N_d increased (Fig. 4(c)). This likely accounts for the minimal current observed in the I–V characteristics of Sample D, which was the most heavily implanted sample (Mg dose of

$1 \times 10^{20} \text{ cm}^{-3}$), as well as the absence of p-type conduction in the Hall-effect measurement. Additionally, this provides a plausible explanation for the previously reported dependence of sheet resistivity on Mg and N doses, where the sheet resistance was higher at an Mg concentration of $9 \times 10^{19} \text{ cm}^{-3}$ than at $2 \times 10^{19} \text{ cm}^{-3}$.²⁰

In summary, Mg and N ions were sequentially implanted into GaN(0001) substrates at equivalent concentrations, followed by annealing at 1300 °C for 60 min. In the Mg dose range of 3×10^{18} – $1 \times 10^{20} \text{ cm}^{-3}$, N_a plateaued at doses above $1 \times 10^{19} \text{ cm}^{-3}$, whereas N_d continued to rise with an increasing Mg dose. Consequently, the net acceptor concentration ($N_a - N_d$) reached a peak of $4 \times 10^{18} \text{ cm}^{-3}$ at an Mg dose of $1 \times 10^{19} \text{ cm}^{-3}$. In addition, ΔE_a decreased with an increasing Mg dose. P-type conduction was not observed in the sample with an Mg dose of $1 \times 10^{20} \text{ cm}^{-3}$. Atomic-resolution structural analysis revealed the formation of nanoscale defects and surrounding Mg-rich clusters, with the peak Mg concentration exceeding 10^{21} cm^{-3} . While the number density of the Mg-rich clusters and peak Mg concentration of these clusters increased with the Mg dose, Mg atoms outside these clusters were uniformly dispersed in the concentration range of 1.3 – $1.5 \times 10^{18} \text{ cm}^{-3}$, independent of the Mg dose. These electrical and structural characterizations indicate that some of the Mg atoms in the Mg-rich clusters acted as acceptors, thereby increasing N_a and net acceptor concentration up to an Mg dose of $1 \times 10^{19} \text{ cm}^{-3}$. These acceptors also contributed to the reduction in the apparent ΔE_a . Meanwhile, other Mg atoms in the clusters likely acted as compensating donors. These donors could have been a cause for the observed increase in N_d , resulting in a decrease in the net acceptor concentration beyond an Mg dose of $1 \times 10^{19} \text{ cm}^{-3}$. These findings clarify the crucial roles of nanoscale implantation defects and dopant clustering in controlling the conductivity of GaN, providing strategic insights into ion-implantation science for semiconductor device technologies.

Supplementary Material

Supplementary Material provides magnified ADF-STEM images of the nanoscale defects in samples A–C (Fig. S1). Fig. S2 shows representative Mg concentration profiles across Mg-rich clusters in these samples, along with their 3D Mg atom maps. Numerical data corresponding to Fig. 2 (total, uniformly distributed, and clustered Mg densities) and Fig. 4(c) (N_a , N_d , and ΔE_a) are listed in Tables S1 and S2, respectively.

Acknowledgment

This work was partly supported by MEXT-Program for Creation of Innovative Core Technology for Power Electronics Grant No. JPJ009777. The APT analysis was supported by Electron Microscopy Unit of National Institute for Materials Science.

Data Availability Statement

The data that supports the findings of this study are available within the article and its supplementary material.

References

- ¹ S.J. Pearton, C.B. Vartuli, J.C. Zolper, C. Yuan, and R.A. Stall, “Ion implantation doping and isolation of GaN,” *Appl. Phys. Lett.* **67**(10), 1435–1437 (1995).
- ² J.C. Zolper, H.H. Tan, J.S. Williams, J. Zou, D.J.H. Cockayne, S.J. Pearton, M.H. Crawford, and R.F. Karlicek, “Electrical and structural analysis of high-dose Si implantation in GaN,” *Appl. Phys. Lett.* **70**(20), 2729–2731 (1997).
- ³ Y. Nakano, and T. Kachi, “Effect of N/Ge co-implantation on the Ge activation in GaN,” *Appl. Phys. Lett.* **79**(10), 1468–1470 (2001).
- ⁴ C. Ronning, “Ion implantation into gallium nitride,” *Phys. Rep.* **351**(5), 349–385 (2001).
- ⁵ B.N. Feigelson, T.J. Anderson, M. Abraham, J.A. Freitas, J.K. Hite, C.R. Eddy, F.J. Kub, and B. Gan, “Multicycle rapid thermal annealing technique and its application for the electrical activation of Mg implanted in GaN,” *J. Cryst. Growth* **350**(1), 21–26 (2012).
- ⁶ J.D. Greenlee, B.N. Feigelson, T.J. Anderson, M.J. Tadjer, J.K. Hite, M.A. Mastro, C.R. Eddy, K.D. Hobart, and F.J. Kub, “Multicycle rapid thermal annealing optimization of Mg-implanted GaN: Evolution of surface, optical, and structural properties,” *J. Appl. Phys.* **116**(6), (2014).
- ⁷ T. Oikawa, Y. Saijo, S. Kato, T. Mishima, and T. Nakamura, “Formation of definite GaN p-n junction by Mg-ion implantation to n--GaN epitaxial layers grown on a high-quality free-standing GaN substrate,” *Nucl. Instruments Methods Phys. Res. Sect. B Beam Interact. with Mater. Atoms* **365**, 168–170 (2015).
- ⁸ T.J. Anderson, J.D. Greenlee, B.N. Feigelson, J.K. Hite, F.J. Kub, and K.D. Hobart, “Improved Vertical GaN Schottky Diodes with Ion Implanted Junction Termination Extension,” *ECS J. Solid State Sci. Technol.* **5**(6), Q176–Q178 (2016).
- ⁹ U. Wahl, L.M. Amorim, V. Augustyns, A. Costa, E. David-Bosne, T.A.L. Lima, G. Lippertz, J.G. Correia, M.R. Da Silva, M.J. Kappers, K. Temst, A. Vantomme, and L.M.C. Pereira, “Lattice Location of Mg in GaN: A Fresh Look at Doping Limitations,” *Phys. Rev. Lett.* **118**(9), 1–6 (2017).
- ¹⁰ T. Narita, T. Kachi, K. Kataoka, and T. Uesugi, “P-type doping of GaN(0001) by magnesium ion implantation,” *Appl. Phys. Express* **10**(1), (2017).
- ¹¹ R. Tanaka, S. Takashima, K. Ueno, H. Matsuyama, and M. Edo, “Demonstration of 1200 V/1.4 mΩ cm² vertical GaN planar MOSFET fabricated by an all ion implantation process,” *Jpn. J. Appl. Phys.* **59**(SG), SGGD02 (2020).
- ¹² H. Sakurai, M. Omori, S. Yamada, Y. Furukawa, H. Suzuki, T. Narita, K. Kataoka, M. Horita, M. Bockowski, J. Suda, and T. Kachi, “Highly effective activation of Mg-implanted p-type GaN by ultra-high-pressure annealing,” *Appl. Phys. Lett.* **115**(14), 1–6 (2019).
- ¹³ T. Kachi, T. Narita, H. Sakurai, M. Matys, K. Kataoka, K. Hirukawa, K. Sumida, M. Horita, N. Ikarashi, K. Sierakowski, M. Bockowski, and J. Suda, “Process engineering of GaN power devices via selective-area p-type doping with ion implantation and ultra-high-pressure annealing,” *J. Appl. Phys.* **132**(13), (2022).

- ¹⁴ K. Hirukawa, K. Sumida, H. Sakurai, H. Fujikura, M. Horita, Y. Otoki, K. Sierakowski, M. Bockowski, T. Kachi, and J. Suda, “Isochronal annealing study of Mg-implanted p-type GaN activated by ultra-highpressure annealing,” *Appl. Phys. Express* **14**(5), (2021).
- ¹⁵ K. Sumida, K. Hirukawa, H. Sakurai, K. Sierakowski, M. Horita, M. Bockowski, T. Kachi, and J. Suda, “Effect of annealing time and pressure on electrical activation and surface morphology of Mg-implanted GaN annealed at 1300 °c in ultra-high-pressure nitrogen ambient,” *Appl. Phys. Express* **14**(12), 121004 (2021).
- ¹⁶ H. Sakurai, T. Narita, M. Omori, S. Yamada, A. Koura, M. Iwinska, K. Kataoka, M. Horita, N. Ikarashi, M. Bockowski, J. Suda, and T. Kachi, “Redistribution of Mg and H atoms in Mg-implanted GaN through ultra-high-pressure annealing,” *Appl. Phys. Express* **13**(8), (2020).
- ¹⁷ T. Narita, H. Yoshida, K. Tomita, K. Kataoka, H. Sakurai, M. Horita, M. Bockowski, N. Ikarashi, J. Suda, T. Kachi, and Y. Tokuda, “Progress on and challenges of p-type formation for GaN power devices,” *J. Appl. Phys.* **128**(9), 090901 (2020).
- ¹⁸ A. Uedono, H. Sakurai, T. Narita, K. Sierakowski, M. Bockowski, J. Suda, S. Ishibashi, S.F. Chichibu, and T. Kachi, “Effects of ultra-high-pressure annealing on characteristics of vacancies in Mg-implanted GaN studied using a monoenergetic positron beam,” *Sci. Rep.* **10**(1), (2020).
- ¹⁹ H. Sakurai, T. Narita, K. Kataoka, K. Hirukawa, K. Sumida, S. Yamada, K. Sierakowski, M. Horita, N. Ikarashi, M. Bockowski, J. Suda, and T. Kachi, “Effects of the sequential implantation of Mg and N ions into GaN for p-type doping,” *Appl. Phys. Express* **14**(11), 0–4 (2021).
- ²⁰ J. Uzuhashi, J. Chen, R. Tanaka, S. Takashima, M. Edo, T. Ohkubo, and T. Sekiguchi, “Effect of sequential N ion implantation in the formation of a shallow Mg-implanted p-type GaN layer,” *J. Appl. Phys.* **136**(5), (2024).
- ²¹ K. Iwata, H. Sakurai, S. Arai, T. Nakashima, T. Narita, K. Kataoka, M. Bockowski, M. Nagao, J. Suda, T. Kachi, and N. Ikarashi, “Defect evolution in Mg ions implanted GaN upon high temperature and ultrahigh N₂ partial pressure annealing: Transmission electron microscopy analysis,” *J. Appl. Phys.* **127**(10), (2020).
- ²² T. Nakashima, E. Kano, K. Kataoka, S. Arai, H. Sakurai, T. Narita, K. Sierakowski, M. Bockowski, M. Nagao, J. Suda, T. Kachi, and N. Ikarashi, “Enhanced activation of Mg ion-implanted GaN at decreasing annealing temperature by prolonging duration,” *Appl. Phys. Express* **14**(1), (2021).
- ²³ E. Kano, K. Kataoka, J. Uzuhashi, K. Chokawa, H. Sakurai, A. Uedono, T. Narita, K. Sierakowski, M. Bockowski, R. Otsuki, K. Kobayashi, Y. Itoh, M. Nagao, T. Ohkubo, K. Hono, J. Suda, T. Kachi, and N. Ikarashi, “Atomic resolution analysis of extended defects and Mg agglomeration in Mg-ion-implanted GaN and their impacts on acceptor formation,” *J. Appl. Phys.* **132**(6), (2022).
- ²⁴ E. Kano, J. Uzuhashi, K. Kobayashi, K. Ishikawa, K. Sawabe, T. Narita, K. Sierakowski, M. Bockowski, T. Ohkubo, T. Kachi, and N. Ikarashi, “Impact of Sequential N Ion Implantation on Extended Defects and Mg Distribution in Mg Ion-Implanted GaN,” *Phys. Status Solidi – Rapid Res. Lett.* **18**(9),

2400074 (2024).

- ²⁵ A. Uedono, H. Sakurai, J. Uzuhashi, T. Narita, K. Sierakowski, S. Ishibashi, S.F. Chichibu, M. Bockowski, J. Suda, T. Ohkubo, N. Ikarashi, K. Hono, and T. Kachi, “Effect of Ultra-High-Pressure Annealing on Defect Reactions in Ion-Implanted GaN Studied by Positron Annihilation,” *Phys. Status Solidi Basic Res.* **259**(10), 1–12 (2022).
- ²⁶ T. Nishimura, and T. Kachi, “Simulation of channeled implantation of magnesium ions in gallium nitride,” *Appl. Phys. Express* **14**(11), 0–4 (2021).
- ²⁷ K. Tsuda, and M. Tanaka, “Refinement of crystal structural parameters using two-dimensional energy-filtered CBED patterns,” *Acta Crystallogr. Sect. A Found. Crystallogr.* **55**(5), 939–954 (1999).
- ²⁸ T. Nagase, K. Chokawa, E. Kano, K. Fukuta, T. Sasaki, S. Fujikawa, M. Takahashi, K. Shiraishi, A. Oshiyama, T. Araki, and N. Ikarashi, “Misfit accommodation in a single interface atomic layer at a highly lattice-mismatched InN/GaN,” *J. Appl. Phys.* **137**(5), 055702 (2025).
- ²⁹ J. Uzuhashi, T. Ohkubo, and K. Hono, “Development of automated tip preparation for atom probe tomography by using script-controlled FIB-SEM,” *Ultramicroscopy* **247**(February), 113704 (2023).
- ³⁰ J. Uzuhashi, and T. Ohkubo, “Systematic study of FIB-induced damage for the high-quality TEM sample preparation,” *Ultramicroscopy* **262**(April), 113980 (2024).
- ³¹ S. Lu, M. Deki, J. Wang, K. Ohnishi, Y. Ando, T. Kumabe, H. Watanabe, S. Nitta, Y. Honda, and H. Amano, “Ohmic contact on low-doping-density p-type GaN with nitrogen-annealed Mg,” *Appl. Phys. Lett.* **119**(24), 242104 (2021).
- ³² K. Sumida, J. Sahashi, K. Sierakowski, T. Sochacki, S. Lu, M. Horita, M. Boćkowski, T. Kachi, and J. Suda, “Ultra-high-pressure annealing with a carbon capping layer as an activation method for Mg-ion-implanted GaN,” *Appl. Phys. Express* **18**(9), 091003 (2025).
- ³³ M. Horita, S. Takashima, R. Tanaka, H. Matsuyama, K. Ueno, M. Edo, T. Takahashi, M. Shimizu, and J. Suda, “Hall-effect measurements of metalorganic vapor-phase epitaxy-grown p-Type homoepitaxial GaN layers with various Mg concentrations,” *Jpn. J. Appl. Phys.* **56**(3), 0–4 (2017).
- ³⁴ P. Kozodoy, H. Xing, S.P. DenBaars, U.K. Mishra, A. Saxler, R. Perrin, S. Elhamri, and W.C. Mitchel, “Heavy doping effects in Mg-doped GaN,” *J. Appl. Phys.* **87**(4), 1832–1835 (2000).
- ³⁵ S. Brochen, J. Brault, S. Chenot, A. Dussaigne, M. Leroux, and B. Damilano, “Dependence of the Mg-related acceptor ionization energy with the acceptor concentration in p-type GaN layers grown by molecular beam epitaxy,” *Appl. Phys. Lett.* **103**(3), 1–5 (2013).
- ³⁶ G. Miceli, and A. Pasquarello, “Self-compensation due to point defects in Mg-doped GaN,” *Phys. Rev. B* **93**(16), 165207 (2016).